*Article*

# Laser–Chemical Surface Treatment for Enhanced Anti-Corrosion and Antibacterial Properties of Magnesium Alloy

Wei Xiong [1,*], Jiajun Fu [2,3], Chao Liu [2,3], Li Li [4,5], Huixin Wang [4,5], Mingjun Zhang [6], Zhiqiang Ge [7], Tairui Zhang [2] and Qinghua Wang [2,3]

[1] Department of Medical, Hunan Traditional Chinese Medical College, Zhuzhou 412012, China
[2] School of Mechanical Engineering, Southeast University, Nanjing 211189, China; 220230419@seu.edu.cn (J.F.); 220220348@seu.edu.cn (C.L.); tairui_zhang@seu.edu.cn (T.Z.); qinghua-wang@seu.edu.cn (Q.W.)
[3] Jiangsu Key Laboratory for Design and Manufacture of Micro-Nano Biomedical Instruments, Nanjing 211189, China
[4] Institute of Agricultural Facilities and Equipment, Jiangsu Academy of Agricultural Sciences, Nanjing 210014, China; muzishuiqudou@163.com (L.L.); wanghuixin@jaas.ac.cn (H.W.)
[5] Key Laboratory of Protected Agriculture Engineering in the Middle and Lower Reaches of Yangtze River, Ministry of Agriculture and Rural Affairs, Nanjing 210014, China
[6] Hunan Provincial Key Laboratory of Intelligent Manufacturing Technology for High-Performance Mechanical Equipment, Changsha University of Science and Technology, Changsha 410114, China; mj_zhang@csust.edu.cn
[7] Special Equipment Safety Supervision Inspection Institute of Jiangsu Province, Nanjing 215128, China; jstj-gzq@foxmail.com
[*] Correspondence: drwei@hhu.edu.cn

**Abstract:** Magnesium (Mg) alloy with good biomechanical and biocompatible properties is considered to be a promising biodegradable material for various applications. However, Mg alloy that is chemically active tends to be corroded in a physiological environment. In this work, we proposed a laser–chemical surface treatment to combine laser surface structuring and stearic immersion treatment to enhance the anti-corrosion and antibacterial properties of Mg alloy. The effects of surface structuring, chemistry, and wettability were analyzed, and the performance of the proposed technique was evaluated in terms of corrosion resistance and antibacterial properties. The experiments showed the following: (1) surface structuring by laser-induced dual-scale micro/nanostructures produced superhydrophilicity, with a water contact angle (WCA) of $0°$ on the surface of the Mg alloy; (2) applying the stearic acid immersion changed the chemistry of the Mg alloy's surface and thus facilitated the wettability transition to superhydrophobicity, with a WCA of $160.1° \pm 0.5°$; (3) the proposed laser–chemical surface treatment enhanced corrosion resistance and stabilized the wettability of Mg alloy in a corrosive medium significantly; and (4) the proposed laser–chemical surface treatment enhanced the antibacterial properties of the Mg alloy greatly, with an improved antibacterial rate as high as 82.05%. This work proved that the proposed laser–chemical surface treatment was a simple, effective, and efficient technique to modulate and control the wettability and further improve the anti-corrosion and antibacterial properties of the Mg alloy.

**Keywords:** magnesium alloy; laser surface structuring; stearic acid treatment; superhydrophobicity; corrosion resistance; antibacterial

## 1. Introduction

Magnesium (Mg) alloy is widely used in biomedical applications due to its distinguishing advantages, such as superior biomechanical properties, good biocompatibility, and high biosafety [1]. Mg-based alloys are promising in their potential to be used as biodegradable materials in surgical implants since their density and elastic modulus are quite similar to those of human cortical bones [2,3]. Using an Mg-based alloy as an implanting material reduces the possibility of stress shielding and avoids secondary surgery [4–7]. On the

other hand, Mg alloys are also chemically active and tend to be corroded in a physiological environment, and this affects the widespread use of Mg alloys as implants [7]. The corrosion and degradation of a Mg alloy can produce hydrogen, increase the pH value of surrounding liquids, and reduce the joining strength of an implant with tissue [8]. Microbiologically induced corrosion also causes the degradation of Mg alloys and, eventually, the failure of the clinical operation [9]. Therefore, it is critical to enhance the anti-corrosion and antibacterial properties of Mg alloys for biomedical applications.

To improve the corrosion resistance or antibacterial properties of a Mg alloy, many techniques have been proposed to treat the surfaces of Mg alloy products. For example, the techniques of physical vapor deposition (PVD) [10,11], chemical vapor deposition (CVD) [12], sol–gel coating [13], conversion coating [14–16], and micro-arc oxidation [17,18] have been developed to improve the corrosion resistance of Mg alloys. The techniques of coating [19–22], microalloying [23], and micro-arc oxidation [24] have been proposed to improve Mg alloys' resistance to bacterial adhesion. Nevertheless, the above-mentioned techniques were coating-based and exhibited some limitations, such as poor reliability, poor durability, a complex coating process, and the possibility of being peeled off. There is an emerging need to develop new surface treatment techniques to improve the corrosion resistance and antibacterial properties of Mg alloys effectively.

Recently, surface structuring via lasers has attracted a great deal of attention due to its potential for automation, environmental friendliness, high flexibility, and the high selectivity of the process [25–29]. Moreover, laser treatment has been combined with sequential surface chemistry treatments to improve the superhydrophobic properties [8,30–32], corrosion resistance [33] and anti-bacterial properties of Mg alloys [34]. For example, Wei et al. [34] prepared a superhydrophobic Mg AZ91 sheet using laser ablation and a subsequent annealing treatment at 160 °C for 60 min. The laser-annealed Mg AZ91 sheet exhibited superhydrophobicity with improved corrosion resistance. Cai et al. [35] laser-textured Mg AZ91D with the structure of a micro-pit array and further immersed the samples into a fluorosilane/ethanol solution to obtain superhydrophobicity. The laser–chemical-treated surface of superhydrophobic Mg AZ91D showed excellent corrosion resistance. Emelyanenko et al. [36] processed superhydrophobic Mg MA8 using a nanosecond laser and CVD with fluorosilane. The corrosion current of the processed Mg MA8 was drastically reduced when it was compared with that of the polished sample. Emelyanenko et al. [9,37] also treated a superhydrophobic Mg alloy with the laser and CVD to suppress the vital activity of bacteria and inhibit the degradation of the substrate of Mg alloy. However, it took 1–2 h for the post-processing treatment, after laser surface texturing, to achieve the wettability transition. Moreover, the fluorosilane reagent was toxic and inapplicable to biomedical applications. It is desirable to develop a bio-friendly and efficient post-processing technique after laser surface treatment that can be used on Mg alloy.

In this work, a novel laser–chemical surface treatment technique was developed in order to prepare the superhydrophobic surface of a Mg alloy, encompassing the following steps: the surface was structured using a laser to induce hierarchical micro/nanostructures to support superhydrophilicity; the surfaces were then processed with stearic acid immersion at 60 °C for 10 min to achieve the wettability transition to superhydrophobicity. Using stearic acid immersion to alter the surface wettability of laser-structured Mg alloy has rarely been reported in the literature. Thus, it can be considered as the key innovative aspect of this work.

To verify the effectiveness of the proposed technique, the morphology of the surface was characterized by a scanning electron microscope (SEM, FEI Sirion, Hillsboro, OR, USA), and the chemistry of the surface was analyzed by energy-dispersive X-ray spectroscopy (EDS, FEI Inspect F50, Hillsboro, OR, USA). The wettability evolution of the surface was demonstrated after each step of the treatment, and the mechanism of the wettability transition was elaborated upon. Finally, the corrosion resistance and antibacterial properties of the treated specimens were evaluated by electrochemical tests and bacterial activity analysis.

## 2. Raw Materials and Methods

### 2.1. Raw Materials

Hot-rolled Mg AZ31B was used as the raw material of specimen in this experiment. The chemical composition of Mg AZ31B is shown in Table 1. Specimens with sizes of $20 \times 20 \times 5$ mm$^3$ and $10 \times 10 \times 5$ mm$^3$ were prepared for the electrochemical and antibacterial tests, respectively. Before the laser–chemical treatment, a specimen with a grit size of 800 was polished by the sandpaper, washed in acetone ultrasonically, and deionized in water successively for 5 min. It was then dried in air for subsequent experiments.

**Table 1.** Chemical composition of Mg AZ31B.

| Element | Al | Zn | Mn | Si | Fe | Cu | Ni | Mg |
|---|---|---|---|---|---|---|---|---|
| wt.% | 2.960 | 0.5200 | 0.310 | 0.160 | 0.003 | 0.006 | 0.001 | Bal. |

### 2.2. Experimental Methods

As shown in Figure 1, the proposed laser–chemical treatment consisted of two steps, i.e., (1) surface structuring using laser and (2) stearic acid immersion. In surface structuring, the laser was produced by the laser marking machine (MQ5T, Mac Laser, Guangzhou, China); it was equipped with a 355 nm UV laser source (Seal-355-3/5, JPT Laser, Shenzhen, China). The UV laser source emitted a laser beam, which passed through the attenuator and beam expander to control the intensity and diameter of laser, respectively. The laser scan head was used to control and modulate the laser beam, which allowed us to structure a two-dimensional surface. The diameter of a focal spot was 50 μm. A cross-hatch surface pattern was adopted to structure surfaces using laser. In Table 2, the key processing parameters of laser surface treatment are listed. This work emphasized the effect of scanning speed and step size on the anti-corrosion and antibacterial properties of treated specimens.
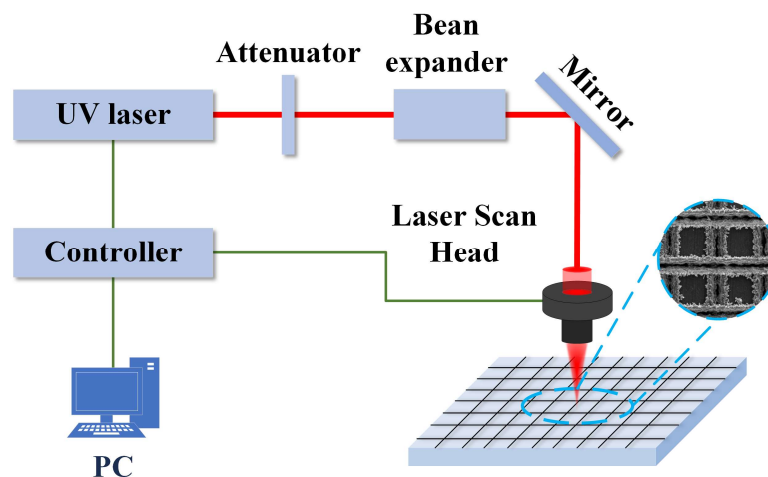


**Figure 1.** Process schematic of laser–chemical treatment.

When a specimen was only treated with laser surface structuring, it typically exhibited superhydrophilicity. To achieve the wettability transition, the laser structured specimen was further immersed in mixed stearic acid (CH$_3$(CH$_2$)$_{16}$COOH with density of 0.9408 g/cm$^3$ and melting point of 69.3 °C)/ethanol (CH$_3$CH$_2$OH) solution at 60 °C with a molar concentration of 0.05 mol/L and a molar ratio of 1:350 for 10 min. The specimen was then cleaned with ethanol to remove excessive stearic acid and dried in ambient air to determine surface properties.

In this study, three types of Mg alloy specimens were prepared and investigated: the first one with untreated surface, the second one with laser surface structuring, and the third one with laser–chemical surface treatment.

**Table 2.** Key parameters of laser processing in laser–chemical treatment.

| Sample No. | 1 | 2 | 3 | 4 | 5 |
|---|---|---|---|---|---|
| Average power (W) | 6.5 | 6.5 | 6.5 | 6.5 | 6.5 |
| Repetition rate (kHz) | 40 | 40 | 40 | 40 | 40 |
| Pulse width (ns) | 12 | 12 | 12 | 12 | 12 |
| Scanning speed (mm/s) | 50 | 100 | 20 | 20 | 20 |
| Step size (μm) | 150 | 150 | 150 | 100 | 200 |
| Power intensity (GW/cm$^2$) | 0.48 | 0.48 | 0.48 | 0.48 | 0.48 |
| Pulse energy (mJ) | 0.2 | 0.2 | 0.2 | 0.2 | 0.2 |

### 2.3. Surface Characterizations

Surface topography/structure and surface chemistry were analyzed by field emission scanning electron microscopy (FE-SEM, FEI Sirion, Hillsboro, OR, USA) and energy-dispersive X-ray spectroscopy (EDS, FEI Inspect F50, Hillsboro, OR, USA), respectively. Water contact angle (WCA) measurements were created by a contact angle goniometer (SCA-100, Mumuxili Technology, Nanjing, China). For each measurement, a 4 μL droplet was dripped onto a specimen, and a high-resolution CMOS camera was used to capture its shape. Five measurements were carried out on each specimen. The averaged value of WCA was analyzed and recorded by ImageJ software.

### 2.4. Electrochemical Tests

Electrochemical tests were employed by using an electrochemical workstation (COR-RTEST CS310X, Wuhan, China) to evaluate the open-circuit potential (OCP), electrochemical impedance spectroscopy (EIS) and potentiodynamic polarization (PDP). A specimen was immersed in the NaCl aqueous solution (3.5 wt%) and tested using a three-electrode cell system. The reference electrode, an Ag/AgCl electrode, was filled with the saturated KCl solution; a graphite electrode was selected as the counter electrode; and a platinum electrode was chosen as the working electrode where the specimen was clamped. The tested area was set at 1 cm$^2$.

A specimen was immersed in the NaCl aqueous solution for 20 min to stabilize OCP before the EIS and PDP tests were performed. The EIS test was implemented by using the following settings: a frequency range of 1~100,000 Hz, a perturbation amplitude of voltage 10 mV, and a recording rate of 30 data points per decade. The results of EIS test were further analyzed by the equivalent circuits. The PDP was conducted using a potential scan rate of 3 mV/s and a potential range of ±0.5 V. Tafel extrapolation was applied to obtain electrochemical parameters, including corrosion potential ($E_{corr}$), corrosion current ($j_{corr}$), and corrosion rate.

### 2.5. Antibacterial Tests

The antibacterial properties of Mg alloy were evaluated using *Escherichia coli* (*E. coli*, ATCC 25922) and *Staphylococcus aureus* (*S. aureus*, ATCC 29213). A specimen was first sterilized using 75 vol% ethanol for 2 h and then dried in air. It was then placed and cleaned ultrasonically in a 24-well plate. Bacterial suspensions of *E. coli* and *S. aureus* (106 CFU/mL) with a volume of 1000 μL were absorbed by pipettes and inoculated on the surface of the specimen. The specimen was then cultured in an incubator at 37 °C for 24 h. After bacteria were adhered to the surface of the specimen, they were completely scraped out by the cotton swabs with phosphate-buffered saline (PBS) in a volume of 1000 μL. Finally, the mixed solution with a volume of 100 μL was absorbed by pipettes, coated on the LB medium, and then cultured at 37 °C for 24 h. The antibacterial rate was calculated by the following equation:

$$\eta_{RA} = \frac{B - A}{B} \times 100\% \tag{1}$$

where the untreated specimen was taken as the reference specimen; $A$ and $B$ are the average numbers of the bacteria colonies in the tested and reference specimens, respectively; and $\eta_{RA}$ is the antibacterial rate.

## 3. Results and Discussion

### 3.1. Surface Structure

Figure 2 shows the micrographs created by SEM with different magnifications from three types of specimens, and the laser–chemical surface treatments used different parameters of laser processing. For the laser-structured specimen, the scanning speed and the step size were set as 20 mm/s and 150 μm, respectively. The surface of the specimen named SHL-150 μm in Figure 2b exhibited superhydrophilicity. For two laser–chemical-treated specimens, the scanning speed was set as 20 mm/s, and the step sizes were set as 150 and 200 μm, respectively. Two specimens, named SHB-150 μm in Figure 2c and SHB-200 μm in Figure 2d, respectively, showed superhydrophobicity. It is clear that the low-magnification (200×) micrograph of the untreated specimen in Figure 2a indicates high flatness and low surface roughness. When a high magnification (1000× or 10,000×) was used, a few horizontally polished marks were observed. After the surface of the specimen was structured by laser, cross-hatch microgrooves under a low magnification were observed on SHL-150 μm [38]. Under high magnification, some sub-microns and nanoparticles were deposited on the top edges of microgrooves, which were caused by the strong ablation and evaporation effect of substrate materials modified by the nanosecond laser [39]. When the scanning speed was increased, a depth change of microgrooves was observed, as shown in Figure S1a,b. When the step size was varied, the density of the cross-hatch structure induced by the laser was changed, as shown in Figure S1c,d. For the laser–chemical-treated specimens, the structures in SHB-150 μm and SHB-200 μm were slightly different from those of SHL-150 μm, as shown in Figure 2c,d. After the specimens were treated by stearic acid immersion, cross-hatch microgrooves were still observable by the SEM under low magnification. Using a high magnification, we uncovered that the number and density of sub-micron and nanoparticles were higher than those of the laser-structured specimen. This was caused by the etching effect of the stearic acid on Mg alloy [1]. When the laser–chemical-treated specimens were observed by varying the scanning speed and step size, a higher density of micro/nanostructures was observed in comparison with the laser-structured specimen, as shown in Figure S2a–c. The results showed that laser structuring induced multi-scale structures on the surface of an Mg alloy specimen effectively and its density could be enhanced further by the stearic acid immersion treatment. Moreover, the structures induced by laser were the key factors in controlling the wettability of Mg alloy specimens [40].

### 3.2. Surface Chemistry

To evaluate the chemistry on the surfaces of three types of specimens, EDS was used for the measurements and analyses, as shown in Figure 3. The results of the untreated specimen are shown in Figure 3a. The elements Mg, aluminum (Al), carbon (C), and oxygen (O) were clearly identified. As shown in Table 1, Al was the primary alloying element for Mg AZ31B, and C and O existed originally in the oxidations and the contamination of the substrate [41]. After the surface was structured by laser, changes in O were detected in SHL-150 μm (Figure 3b), and the atomic percentage (at%) was increased from 2.05% to 32.52%. Such an increase was also visible in the EDS mapping data of element O. This indicated that laser surface structuring not only produced cross-hatch microgrooves but also oxidized the surface of the specimen significantly, which helped to produce a large amount of OH and -COOH for high polarity [42,43]. When the laser-structured specimen was observed by SEM at different scanning speeds and step sizes, changes in O were observed, as shown in Figure S3a,b. As shown in Figure 3c,d, after the specimens were treated with the stearic acid immersion, the atomic percentage of C was increased on the surfaces of SHB-150 μm and SHB-150 μm Mg alloy in comparison with SHL-150 μm. The

EDS mapping data of C for the laser–chemical-treated specimen also exhibited a significant increase in carbon content; the change in C was observable in Figure S3c, even though the scanning speeds were different. The results showed that the long-chain molecules in stearic acid ($CH_3(CH_2)_{16}COO_-$) were bonded onto the surface of the specimen successfully and firmly [44]. It was also seen that magnesium stearate $Mg[CH_3(CH2)_{16}COO]_2$ was formed on laser–chemical-treated specimen under low surface energy [43]. The measurements and analyses of EDS showed that both laser surface structuring and stearic acid immersion were able to change the chemistry on the surface of an Mg alloy, which was another important factor used to control and regulate its wettability [40].
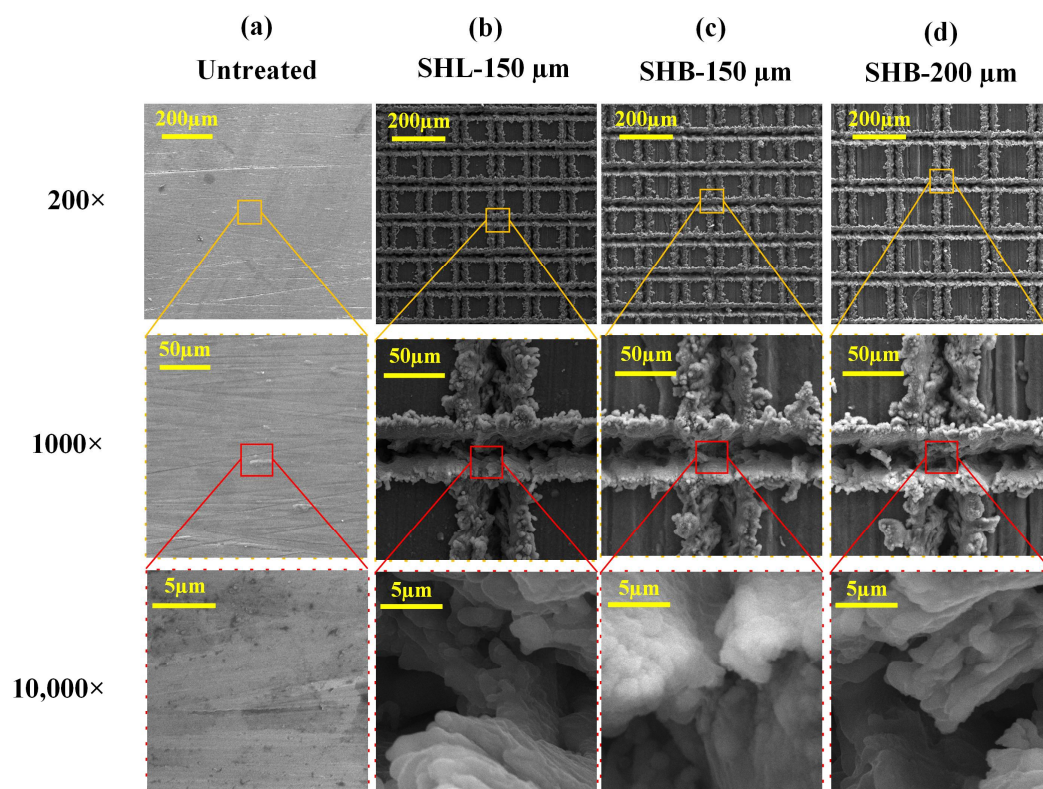


**Figure 2.** SEM micrographs for the Mg alloy surfaces treated by different methods: (**a**) untreated; (**b**) SHL-150 μm; (**c**) SHB-150 μm; (**d**) SHB-200 μm.

### 3.3. Surface Wettability

Figure 4 shows the evolution of the surface wettability of a specimen after each treatment. The untreated specimen with a WCA of 69.8° ± 0.6° exhibited hydrophilicity. Immediately after laser surface structuring treatment, the specimen with WCA reduced to 0° drastically became superhydrophilic. This was caused by two factors: (1) the increased surface roughness led to the saturated Wenzel state of droplets on the surface; which, in turn, resulted in superhydrophilicity [42]; (2) a large amount of −OH and −COOH was generated to promote the superhydrophilicity of the surface [41]. The WCA of the laser–chemical-treated specimen was increased significantly to 160.1° ± 0.5°, indicating that the surface of the specimen was superhydrophobic. The results showed that immersion in the mixed stearic acid/ethanol solution was conducive to reducing the surface energy effectively [43,45,46]. With the combined effect of low surface energy and laser-induced surface structure, the superhydrophilicity was transited into superhydrophobicity successfully.
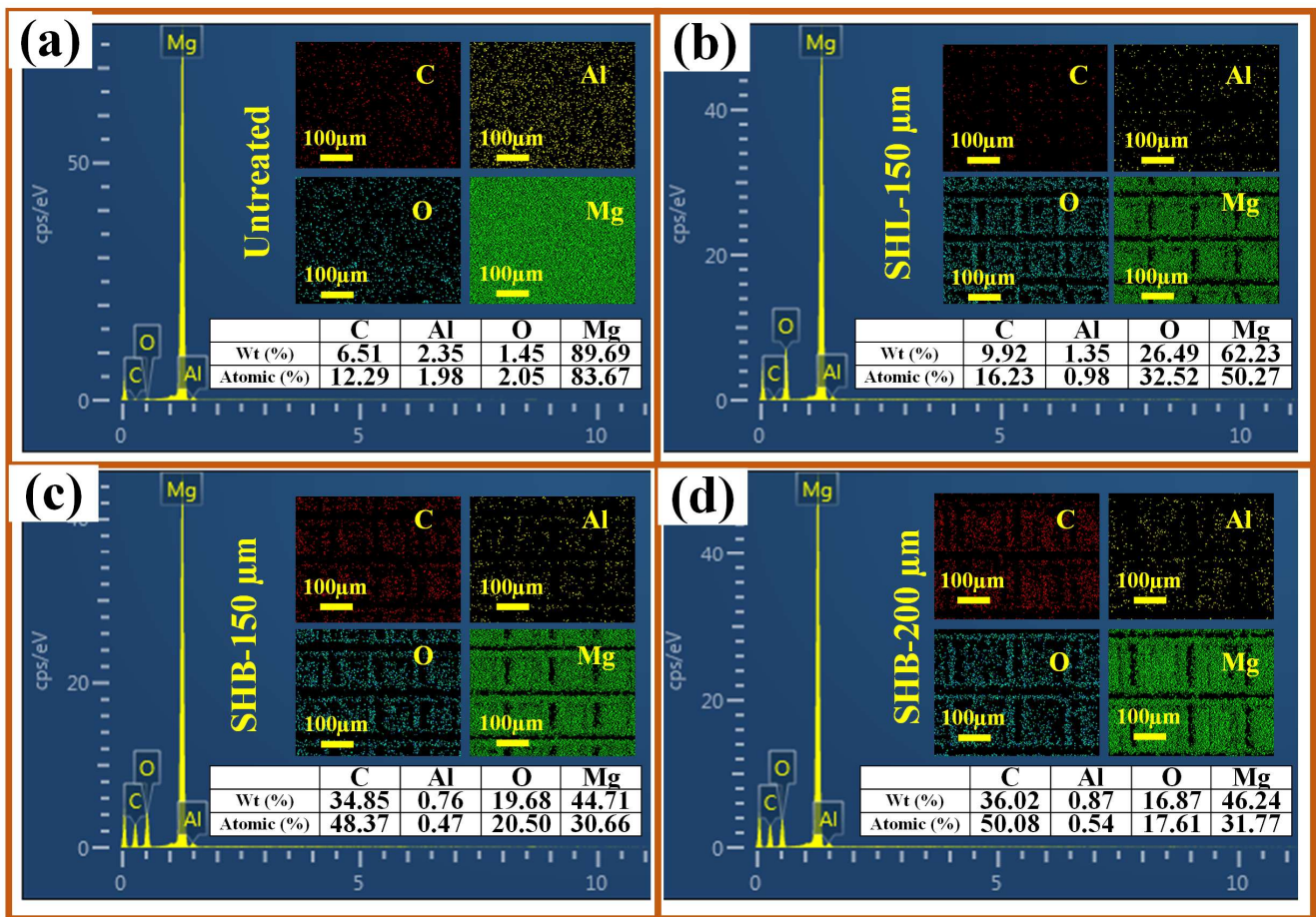
**Figure 3.** EDS analyses of four specimens: (**a**) untreated; (**b**) SHL-150 μm; (**c**) SHB-150 μm; (**d**) SHB-200 μm.
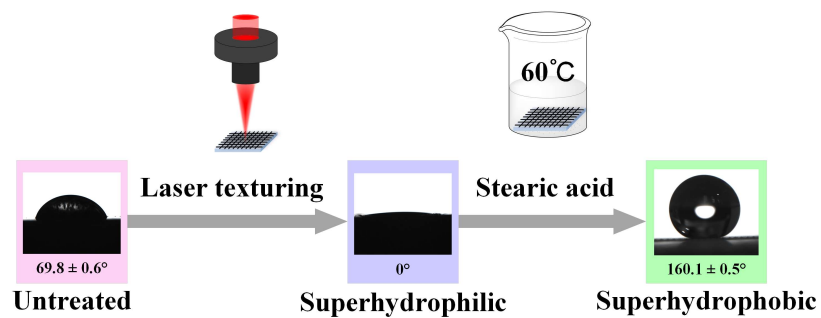


**Figure 4.** Evolution of surface wettability of a specimen after each treatment.

As shown in Table 2, when the scanning speed was changed, the step size was kept constant at 150 μm; in turn, when the step size was changed, the scanning speed was kept constant at 20 mm/s. Figure 5 illustrates the WCA of the laser–chemical-treated specimens that were processed at different scanning speeds and step sizes. Figure 5a shows that at a scanning speed of 20 or 50 mm/s, the surface of the laser–chemical-treated specimen exhibited distinct superhydrophobicity; when the scanning speed rose to 100 mm/s, the WCA dropped to slightly below 150°, but it still maintained high hydrophobicity. The main reason for this result was that a high scanning speed lowered the time of laser–material interaction and thus weakened the density of surface micro/nanostructures, as shown in Figure S2, leading to a slight decrease in the WCA. For step sizes from 100 to 200 μm that were tested here, the superhydrophobicity was stabilized, and a wide scope of effective processing variables in the laser–chemical treatment is depicted in Figure 5b. The results

show clearly that laser processing parameters could be selected to modulate and control the wettability of the surface appropriately.
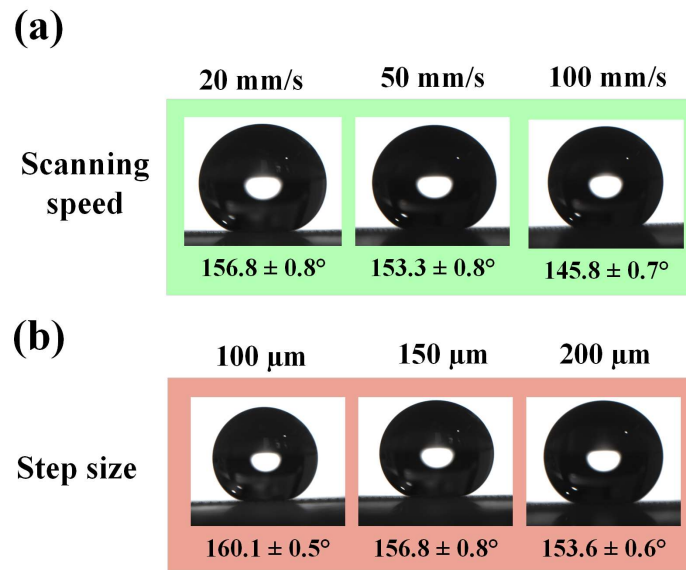
**(a)**



**(b)**



**Figure 5.** WCA of laser–chemical-treated specimens with (**a**) different scanning speeds and (**b**) different step sizes.

### 3.4. Corrosion Resistance

The corrosion of three types of specimens was characterized by electrochemical tests. The OCP curves in Figure 6a indicate that the OCP value of SHL-150 μm was slightly larger than that of the untreated specimen, implying that the laser surface structuring had an insignificant effect in improving corrosion resistance. In contrast, both SHB-150 μm and SHB-200 μm yielded a larger OCP, suggesting that the corrosion resistance was significantly improved [47,48]. The PDP curves in Figure 6b further backed up the enhanced corrosion resistance. Compared with that of the untreated specimen, the PDP curve of both SHB-150 μm and SHB-200 μm deviated in the direction of positive potential. As shown in Table 3, the corresponding $E_{corr}$ values were much higher, and $j_{corr}$ values were several orders lower than those of the untreated specimen. The corrosion rate of SHB-150 μm and SHB-200 μm was much lower than that of the untreated specimen, which confirmed that the corrosion resistance of the Mg alloy with superhydrophobicity was enhanced by the laser–chemical surface treatment [49]. However, the PDP curve of SHL-150 μm deviated toward the direction of negative potential, and that of $E_{corr}$, $j_{corr}$, and corrosion rate were worsened, indicating that the corrosion resistance was not improved.
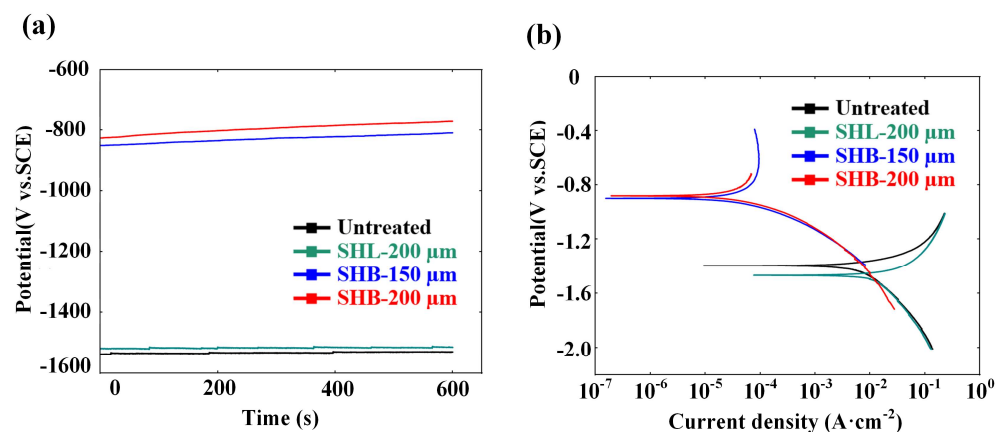
**(a)**                    **(b)**



**Figure 6.** OCP and PDP curves of three types of specimens.

**Table 3.** Corrosion potential, corrosion current density, and corrosion rate of specimens in 3.5 wt% NaCl solution.

| Sample Type | Corrosion Potential, $E_{corr}$ (mv) | Current Density, $j_{corr}$ (A/cm$^2$) | Corrosion Rate (mm/a) |
|---|---|---|---|
| Untreated | −1397.5 | 0.015 | 179.81 |
| SHL-150 | −1469.7 | 0.038 | 446.8 |
| SHB-150 | −898.5 | $8.3 \times 10^{-5}$ | 0.9728 |
| SHB-200 | −880.1 | $8.7 \times 10^{-5}$ | 1.0399 |

Figure 7a–c show the EIS spectra of specimens. The Nyquist plots in Figure 7a show that the semi-circle diameter of the capacitive loop of SHB-150 μm and SHB-200 μm was larger than that of the untreated specimen; however, the diameter of SHL-150 μm was smaller than that of the untreated specimen. The results are consistent with the comparison of the OCP and PDP curves, which show that the corrosion resistance was improved in SHB-150 μm and SHB-200 μm but worsened in SHL-150 μm [47,48]. The Bode impedance plots in Figure 7b show that the impedance value (|Z|) of SHB-150 μm and SHB-200 μm Mg alloy was higher than that of the untreated specimen. The Bode phase plots in Figure 7c illustrate that the phase angle of SHB-150 μm and SHB-200 μm was higher than that of untreated specimens at a high-frequency range of over 1000 Hz. Higher |Z| values and phase angles indicate the significant enhancement in the corrosion resistance created by the proposed laser–chemical surface treatment [50,51].
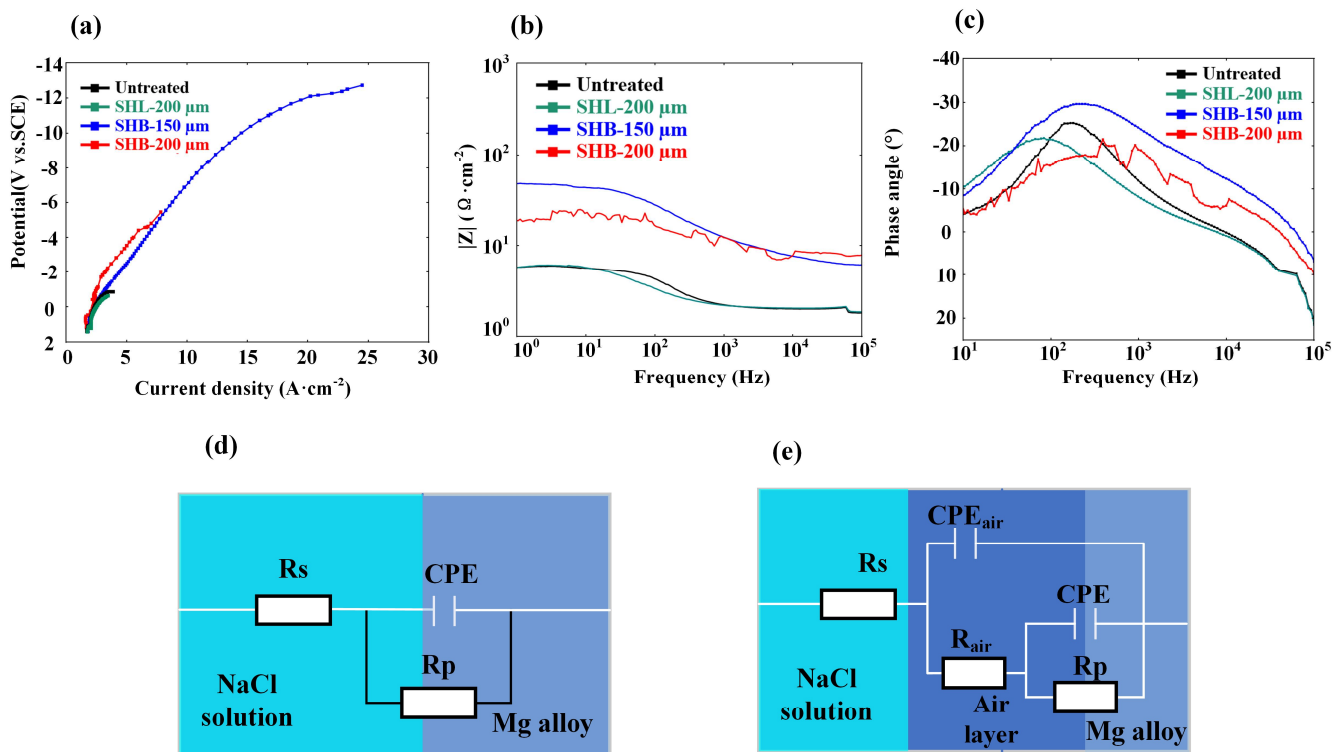


**Figure 7.** EIS spectra and EEC model of specimens: (**a**) Nyquist plots; (**b**) Bode impedance plots; (**c**) Bode phase plots; (**d**) Untreated EEC model; (**e**) Superhydrophobic EEC model.

An equivalent electric circuit (EEC) model consisting of solution resistance ($R_s$), polarization resistance ($R_p$), and double-layer capacitance ($C_{dl}$) was utilized to analyze the EIS data, as shown in Figure 7d (untreated model) and 7e (superhydrophobic model). Compared with the untreated model, the superhydrophobic model exhibited an obvious air layer that could prevent contact between the Mg alloy surface and electrolyte to improve

corrosion resistance. In Table 4, the fitting data are depicted. $R_s$ and $R_p$ of SHB-150 μm, 6.214 and 45.968 Ω·cm$^2$, were 212% and 1266% times higher than those of the untreated specimen, respectively. Meanwhile, in comparison with that of the untreated specimen, $C_{dl}$ was reduced to $1.194 \times 10^{-4}$ S·sn/cm$^2$. Compared with those of the untreated specimen, $R_s$ and $R_p$ of SHB-200 μm were slightly lower, and $C_{dl}$ was slightly higher, which still showed an improvement. Larger $R_s$ and $R_p$ and smaller $C_{dl}$ represented a slow corrosion rate [52]. The fitting data of the EEC model confirmed the enhanced corrosion resistance of the proposed laser–chemical surface treatment.

**Table 4.** Equivalent EEC elements derived from the fitted EIS data.

| Sample Type | Solution Resistance $R_s$ (Ω·cm$^2$) | Polarization Resistance $R_p$ (Ω·cm$^2$) | Double-Layer Capacitance $C_{dl}$ (S·sn·cm$^{-2}$) |
|---|---|---|---|
| Untreated | 1.9921 | 3.364 | $5.419 \times 10^{-4}$ |
| SHL-150 | 2.0388 | 3.1944 | $13.29 \times 10^{-4}$ |
| SHB-150 | 6.214 | 45.968 | $1.194 \times 10^{-4}$ |
| SHB-200 | 4.797 | 35.178 | $3.851 \times 10^{-4}$ |

To further quantify the anti-corrosion capability of specimens under a corrosive condition, the variation in surface structure, chemistry, and wettability of specimens was examined while referring to previous work [53]. As shown in Figure 8a,b, a large number of black corrosion pits was observed on the untreated and SHL-150 μm specimens. The surfaces on these two specimens were roughened severely, and the surface patterns were damaged to some extent. In Figure 8c,d, no pit can be observed on SHB-150 μm and SHB-200 μm specimens, but some corrosion occurs in a few specific areas, indicating that the surface by laser–chemical treatment was well preserved. It was worth noting that the superhydrophobic surface was obtained after stearic acid immersion treatment and blocked the attack of chloride ions (Cl$^-$) effectively [43]. Figure 9 shows a schematic illustration of the enhancement in anti-corrosion capability created by laser–chemical surface treatment.

In the EDS spectra, the atomic percentages of element O in the untreated and SHL-150 μm specimens increased considerably, indicating that for electrochemical corrosion, the hydrogen reaction in the NaCl electrolytic cell generated Mg(OH)$_2$ on their surface [54,55]. The elements Na and Cl, with relatively high atomic percentages, were also detected on the untreated and SHL-150 μm specimens, which was caused by the hydrophilicity of the specimens. Corrosive Cl$^-$ tended to contact and penetrate the surface and caused severe corrosion [49], which mainly led to corrosion of the untreated and laser-structured specimens. The atomic percentages of O in SHB-150 μm and SHB-200 μm specimens slightly increased after the electrochemical tests, and the contents of Na and Cl were much lower than those of the untreated or SHL-150 μm specimen, which was attributed to (1) the superhydrophobic nature of the surface and (2) the air layer induced by dual-scale micro/nanostructures that avoided direct contact of corrosive ions with the surface of the specimen (Figure 9) [8,30]. It was shown that the laser–chemical treatment enhanced the resistance to Cl$^-$ and weakened electrochemical corrosions. The EDS results proved the effectiveness of the proposed laser–chemical surface treatment in improving corrosion resistance.
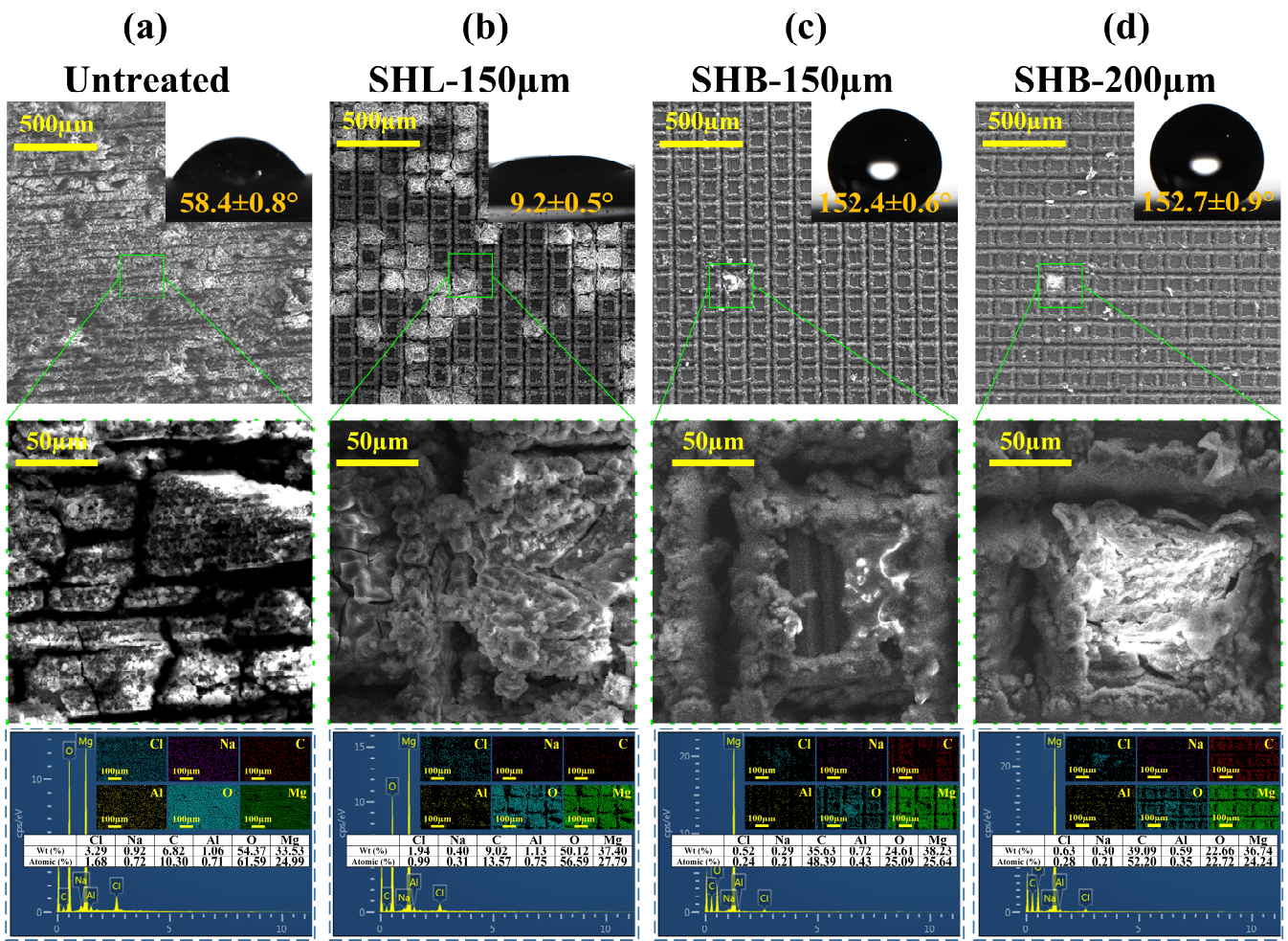
**Figure 8.** SEM micrographs, EDS spectra, and wettability for specimens after laser–chemical surface treatment: (**a**) untreated; (**b**) SHL-150 μm; (**c**) SHB-150 μm; (**d**) SHB-200 μm.
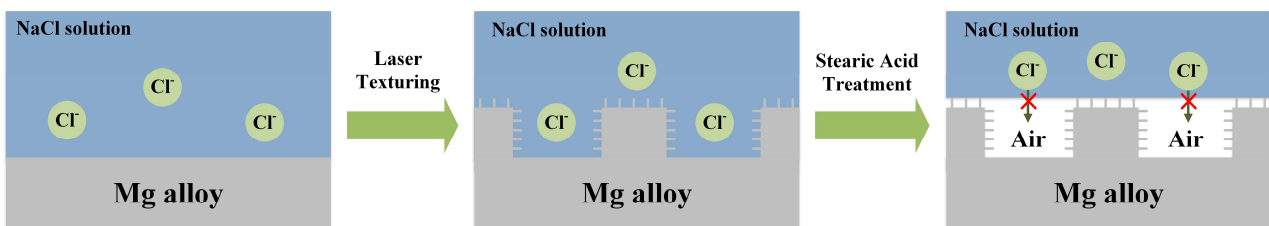


**Figure 9.** Schematic illustration of enhancement of anti-corrosion using laser–chemical surface treatment.

### 3.5. Antibacterial Property

Figure 10 shows high-resolution images of bacteria colonies of specimens cultured for 24 h. The antibacterial performance was evaluated by the number of bacteria colonies. A large number of *E. coli* and *S. aureus* colonies were observed on the untreated specimen, indicating its poor antibacterial performance. Immediately after the surface was structured by a laser, the numbers of *E. coli* and *S. aureus* colonies of SHL-150 μm increased slightly. This indicated that the laser structuring on the surface with superhydrophilicity did not change its antibacterial performance effectively. However, the numbers of *E. coli* and *S. aureus* colonies of SHB-150 μm in the laser–chemical surface treatment were reduced significantly, which proved that the proposed laser–chemical surface treatment improved the antibacterial performance remarkably.
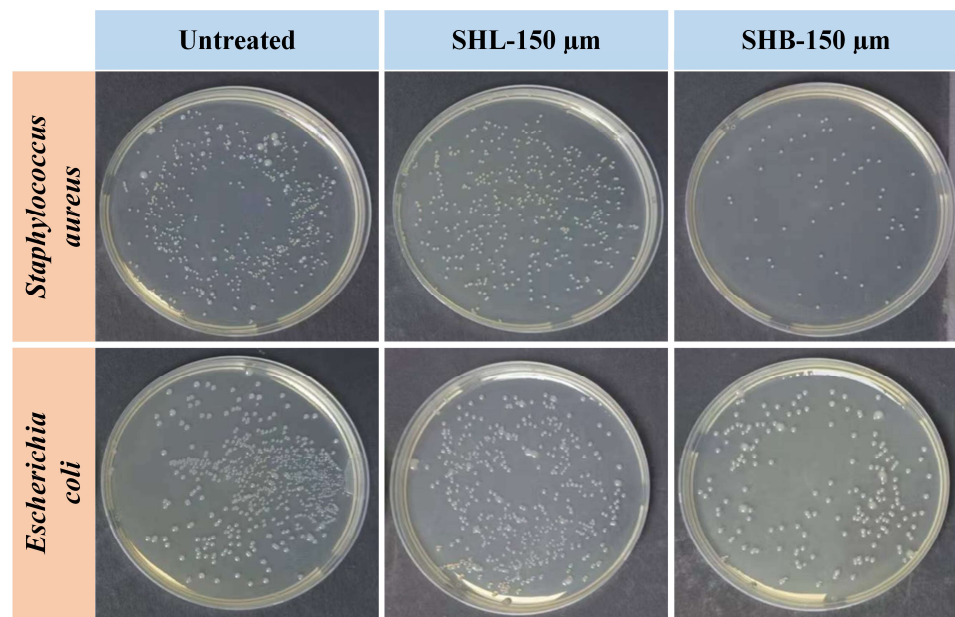
**Figure 10.** Images of bacteria on tested specimens.

Equation (1) was used to calculate the antibacterial rate of the laser-structured and laser–chemical-treated specimens based on China's standard GB/T 2591 [56], as shown in Figure 11. The antibacterial rate of *E. coli* in SHL-150 μm was merely 8.22%, while it increased greatly to 74.43% in SHB-150 μm. The antibacterial rates of *S. aureus* in SHL-150 μm and SHB-150 μm were 8.01% and 82.05%, respectively. The big difference in antibacterial rates in these specimens showed that the laser–chemical surface treatment induced superhydrophobicity and improved the antibacterial performance of Mg alloy significantly [36,37].
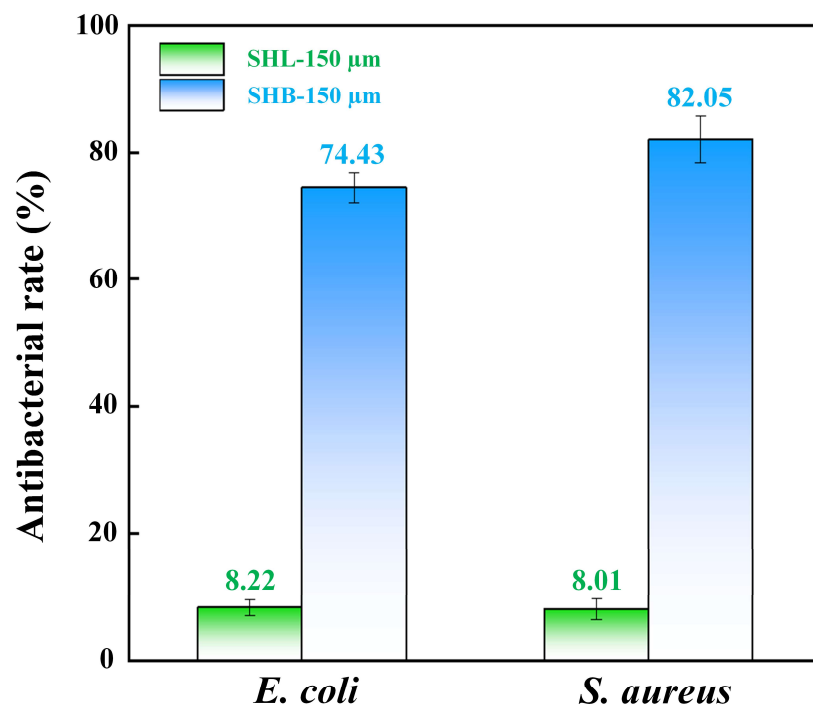


**Figure 11.** Antibacterial rates of tested specimens.

Figure 12 illustrates the mechanism used to enhance the antibacterial performance in the laser–chemical surface treatment. The untreated specimen was hydrophilic; therefore,

the bacterial fluid could spread easily and facilitate bacterial adhesion on the surface [51,57]. The surface of specimens was structured by a laser, and microgrooves with sub-micron and nanoparticles were formed to reduce bacterial adhesion, thereby lowering the antibacterial rate [58,59]. However, since the laser-structured surface exhibited superhydrophilicity, the bacterial fluid was still able to penetrate into the surface and cause significant bacterial adhesion. When the surface was laser–chemical-treated, the structured surface with super-hydrophobicity could form air pockets to prevent the penetration of bacterial fluid and the direct contact of bacterial cells with the surface [60]. Therefore, both the bacterial adhesion and antibacterial rate were reduced greatly by the laser–chemical surface treatment.
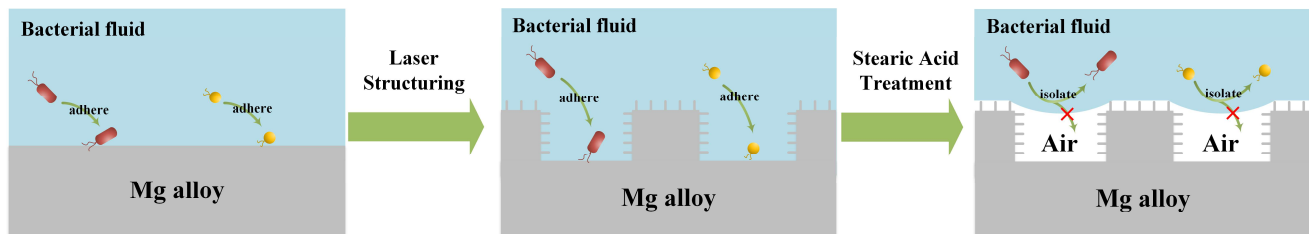


**Figure 12.** Schematic illustration of the underlying mechanism of bacterial adhesion on different types of Mg alloy surfaces.

## 4. Conclusions

In this paper, a simple and efficient laser–chemical surface treatment was proposed to functionalize the surface of the Mg alloy specimen, and relevant experiments were conducted to verify its effectiveness. In particular, electrochemical and antibacterial tests were carried out to evaluate the corrosion resistance and antibacterial performance of specimens in comparative studies. The following conclusions were drawn:

1. Laser surface structuring was used to generate dual-scale micro/nanostructures on the surface of a Mg alloy specimen due to the strong ablation and evaporation in laser–material interaction.
2. The stearic acid immersion improved the deposition and bonding of long-chain molecules on the surface of Mg alloy specimens in the stearic acid and reduced the surface energy significantly.
3. By incorporating the effect of dual-scale micro/nanostructures, the superhydrophilicity on the surface could be transited into superhydrophobicity via sequential chemical immersion.
4. Compared with that of the untreated specimen, the corrosion resistance of laser–chemical-treated specimen was enhanced significantly, which was attributed to its superhydrophobicity in that the structure-induced air layer prevented the direct contact of corrosive ions with the surface of the specimen.
5. The proposed laser–chemical surface treatment also strengthened the antibacterial performance of the Mg alloy specimen greatly, and the antibacterial rate was as high as 82.05%, mainly owing to the air pockets in the structured surface restraining the penetration of bacterial fluid.

a scanning speed of 20 mm/s and step size of 200 μm; (c) laser–chemical-treated Mg alloy surface processed with a scanning speed of 100 mm/s and step size of 150 μm.

**Institutional Review Board Statement:** Not applicable.

**Informed Consent Statement:** Not applicable.

**Data Availability Statement:** Data will be available upon request.

**Conflicts of Interest:** The authors declare no conflicts of interest.

# References

1. Sezer, N.; Evis, Z.; Murat, S.; Tahmasebifar, A.; Koç, M. Review of magnesium-based biomaterials and their applications. *J. Magnes. Alloys* **2018**, *6*, 23–43. [CrossRef]
2. Witte, F. The history of biodegradable magnesium implants: A review. *Acta Biomater.* **2010**, *6*, 1680–1692. [CrossRef]
3. Witte, F.; Fischer, J.; Nellesen, J.; Crostack, H.; Kaese, V.; Pisch, A.; Beckmann, F.; Windhagen, H. In vitro and in vivo corrosion measurements of magnesium alloys. *Biomaterials* **2006**, *27*, 1013–1018. [CrossRef] [PubMed]
4. Staiger, M.P.; Pietak, A.M.; Huadmai, J.; Dias, G. Magnesium and its alloys as orthopedic biomaterials: A review. *Biomaterials* **2006**, *27*, 1728–1734. [CrossRef] [PubMed]
5. Song, G. Control of biodegradation of biocompatable magnesium alloys. *Corros. Sci.* **2007**, *49*, 1696–1701. [CrossRef]
6. Castellani, C.; Lindtner, R.A.; Hausbrandt, P.; Tschegg, E.; Stanzl-Tschegg, S.E.; Zanoni, G.; Beck, S.; Weinberg, A.M. Bone-implant interface strength and osseointegration: Biodegradable magnesium alloy versus standard titanium control. *Acta Biomater.* **2011**, *7*, 432–440. [CrossRef] [PubMed]
7. Kirkland, N.T.; Lespagnol, J.; Birbilis, N.; Staiger, M.P. A survey of bio-corrosion rates of magnesium alloys. *Corros. Sci.* **2010**, *52*, 287–291. [CrossRef]
8. Liu, H.; Tong, Z.; Gu, J.; Yang, D.; Liu, C.; Wang, X.; Ren, X. Effect of laser surface texturing depth and pattern on the bond strength and corrosion performance of phosphate conversion coating on magnesium alloy. *Opt. Laser Technol.* **2022**, *153*, 108164. [CrossRef]
9. Emelyanenko, A.M.; Domantovsky, A.G.; Kaminsky, V.V.; Pytskii, I.S.; Emelyanenko, K.A.; Boinovich, L.B. The mechanisms of antibacterial activity of magnesium alloys with extreme wettability. *Materials* **2021**, *14*, 5454. [CrossRef] [PubMed]
10. Wu, G.; Zeng, X.; Yuan, G. Growth and corrosion of aluminum PVD-coating on AZ31 magnesium alloy. *Mater. Lett.* **2008**, *62*, 4325–4327. [CrossRef]
11. Hollstein, F.; Wiedemann, R.; Scholz, J. Characteristics of PVD-coatings on AZ31hp magnesium alloys. *Surf. Coat. Technol.* **2003**, *162*, 261–268. [CrossRef]
12. Christoglou, C.; Voudouris, N.; Angelopoulos, G.N.; Pant, M.; Dahl, W. Deposition of aluminium on magnesium by a CVD process. *Surf. Coat. Technol.* **2004**, *184*, 149–155. [CrossRef]
13. Tan AL, K.; Soutar, A.M.; Annergren, I.F.; Liu, Y.N. Multilayer sol-gel coatings for corrosion protection of magnesium. *Surf. Coat. Technol.* **2005**, *198*, 478–482. [CrossRef]
14. Huo, H.; Li, Y.; Wang, F. Corrosion of AZ91D magnesium alloy with a chemical conversion coating and electroless nickel layer. *Corros. Sci.* **2004**, *46*, 1467–1477. [CrossRef]
15. Guo, L.; Gu, C.; Zhang, J.; Wang, X.; Wang, K.; Jin, Y.; Tu, J. A black conversion coating produced by hot corrosion of magnesium with deep eutectic solvent membrane. *Surf. Coat. Technol.* **2019**, *357*, 833–840. [CrossRef]
16. Chiu, K.Y.; Wong, M.H.; Cheng, F.T.; Man, H.C. Characterization and corrosion studies of fluoride conversion coating on degradable Mg implants. *Surf. Coat. Technol.* **2007**, *202*, 590–598. [CrossRef]
17. Cui, X.; Lin, X.; Liu, C.; Yang, R.; Zheng, X.; Gong, M. Fabrication and corrosion resistance of a hydrophobic micro-arc oxidation coating on AZ31 Mg alloy. *Corros. Sci.* **2015**, *90*, 402–412. [CrossRef]
18. Duan, H.; Du, K.; Yan, C.; Wang, F. Electrochemical corrosion behavior of composite coatings of sealed MAO film on magnesium alloy AZ91D. *Electrochim. Acta* **2006**, *51*, 2898–2908. [CrossRef]

19. Gnedenkov, A.S.; Sinebryukhov, S.L.; Filonina, V.S.; Plekhova, N.G.; Gnedenkov, S.V. Smart composite antibacterial coatings with active corrosion protection of magnesium alloys. *J. Magnes. Alloys* **2022**, *10*, 3589–3611. [CrossRef]

20. Mehrjou, B.; Dehghan-Baniani, D.; Shi, M.; Shanaghi, A.; Wang, G.; Liu, L.; Qasim, A.M.; Chu, P.K. Nanopatterned silk-coated AZ31 magnesium alloy with enhanced antibacterial and corrosion properties. *Mater. Sci. Eng. C* **2020**, *116*, 111173. [CrossRef] [PubMed]

21. Zou, Y.-H.; Wang, J.; Cui, L.-Y.; Zeng, R.-C.; Wang, Q.-Z.; Han, Q.-X.; Qiu, J.; Chen, X.-B.; Chen, D.-C.; Guan, S.-K.; et al. Corrosion resistance and antibacterial activity of zinc-loaded montmorillonite coatings on biodegradable magnesium alloy AZ31. *Acta Biomater.* **2019**, *98*, 196–214. [CrossRef]

22. Tamurejo-Alonso, P.; Luisa González-Martín, M.; Pacha-Olivenza, M.A. Coating of a biodegradable magnesium alloy for rapid action against S. aureus after ultraviolet exposition. *Appl. Surf. Sci.* **2023**, *613*, 156006.

23. Gao, Z.; Song, M.; Liu, R.-L.; Shen, Y.; Ward, L.; Cole, I.; Chen, X.-B.; Liu, X. Improving in vitro and in vivo antibacterial functionality of Mg alloys through micro-alloying with Sr and Ga. *Mater. Sci. Eng. C* **2019**, *104*, 109926. [CrossRef]

24. Yan, X.; Zhao, M.-C.; Yang, Y.; Tan, L.; Zhao, Y.-C.; Yin, D.-F. Improvement of biodegradable and antibacterial properties by solution treatment and micro-arc oxidation (MAO) of a magnesium alloy with a trace of copper. *Corros. Sci.* **2019**, *156*, 125–138. [CrossRef]

25. Wang, H.; Wang, Q.; Huo, L.; Liu, J.; Bai, Z. High-efficient laser-based bionic surface structuring for enhanced surface functionalization and self-cleaning effect. *Surf. Interfaces* **2023**, *37*, 102691. [CrossRef]

26. Wang, L.; Yin, K.; Deng, Q.; Huang, Q.; He, J.; Duan, J. Wetting Ridge-Guided Directional Water Self-Transport. *Adv. Sci.* **2022**, *9*, 2204891. [CrossRef] [PubMed]

27. Wang, Q.; Wang, H. Laser surface functionalization to achieve extreme surface wetting conditions and resultant surface functionalities. *J. Cent. South Univ.* **2022**, *29*, 3217–3247. [CrossRef]

28. Kozera, R.; Przybyszewski, B.; Krawczyk, Z.D.; Boczkowska, A.; Sztorch, B.; Przekop, R.E.; Barbucha, R.; Tański, M.; Casas, X.G.; Borras, A. Hydrophobic and anti-icing behavior of uv-laser-treated polyester resin-based gelcoats. *Processes* **2020**, *8*, 1642. [CrossRef]

29. Ahuir-Torres, J.I.; Kotadia, H.R.; Öpoz, T.T.; Sharp, M.C. A Study on the Corrosion Behaviour of Laser Textured Pure Aluminium in Saltwater. *Processes* **2023**, *11*, 721. [CrossRef]

30. Liu, H.; Tong, Z.; Yang, Y.; Zhou, W.; Chen, J.; Pan, X.; Ren, X. Preparation of phosphate conversion coating on laser surface textured surface to improve corrosion performance of magnesium alloy. *J. Alloys Compd.* **2021**, *865*, 158701. [CrossRef]

31. Ma, C.; Peng, G.; Nie, L.; Liu, H.; Guan, Y. Laser surface modification of Mg-Gd-Ca alloy for corrosion resistance and biocompatibility enhancement. *Appl. Surf. Sci.* **2018**, *445*, 211–216. [CrossRef]

32. Liang, M.; Yuan, Y.; Li, X.; Cheng, J.; Zhang, X.; Zhang, K.; You, R. Enhanced corrosion resistance of Mg and Mg alloys with fs-laser printed hydrophobic and periodically microrippled surface for armor application. *Appl. Surf. Sci.* **2023**, *639*, 158156. [CrossRef]

33. Zhao, W.; Cao, Q.; Hu, J. Response surface and corrosion behavior analysis of nanosecond laser patterned ZK60A magnesium alloy. *Opt. Laser Technol.* **2022**, *145*, 107501. [CrossRef]

34. Pacha-Olivenza, M.A.; Galván, J.C.; Porro, J.A.; Lieblich, M.; Díaz, M.; Angulo, I.; Cordovilla, F.; García-Galván, F.R.; Fernández-Calderón, M.C.; González-Martín, M.L.; et al. Efficacy of laser shock processing of biodegradable Mg and Mg-1Zn alloy on their in vitro corrosion and bacterial response. *Surf. Coat. Technol.* **2020**, *384*, 125320. [CrossRef]

35. Cai, Q.; Xu, J.; Lian, Z.; Yu, Z.; Yu, H.; Li, J. Superhydrophobic magnesium alloy surface with corrosion resistance. In Proceedings of the IEEE International Conference on Manipulation, Manufacturing and Measurement on the Nanoscale, 3M-NANO 2021—Proceedings, Xi'an, China, 2–6 August 2021; pp. 328–331.

36. Emelyanenko, K.A.; Chulkova, E.V.; Semiletov, A.M.; Domantovsky, A.G.; Palacheva, V.V.; Emelyanenko, A.M.; Boinovich, L.B. The Potential of the Superhydrophobic State to Protect Magnesium Alloy against Corrosion. *Coatings* **2022**, *12*, 74. [CrossRef]

37. Emelyanenko, A.M.; Kaminsky, V.V.; Pytskii, I.S.; Emelyanenko, K.A.; Domantovsky, A.G.; Chulkova, E.V.; Shiryaev, A.A.; Aleshkin, A.V.; Boinovich, L.B. Antimicrobial activity and degradation of superhydrophobic magnesium substrates in bacterial media. *Metals* **2021**, *11*, 1100. [CrossRef]

38. Furlan, V.; Biondi, M.; Demir, A.G.; Pariani, G.; Previtali, B.; Bianco, A. Sub-micrometric surface texturing of AZ31 Mg-alloy through two-beam direct laser interference patterning with a ns-pulsed green fiber laser. *Appl. Surf. Sci.* **2017**, *423*, 619–629. [CrossRef]

39. Khadka, I.; Castagne, S.; Wang, Z.; Zheng, H. Surface structure formation in WE54 Mg alloy subjected to ultrafast laser texturing. *J. Laser Appl.* **2016**, *28*, 022504. [CrossRef]

40. Samanta, A.; Wang, Q.; Shaw, S.K.; Ding, H. Roles of chemistry modification for laser textured metal alloys to achieve extreme surface wetting behaviors. *Mater. Des.* **2020**, *192*, 108744. [CrossRef]

41. Wang, Q.; Zhou, Y.; Wu, P.; Qu, C.; Wang, H. Effect of Laser Surface Structuring on Surface Wettability and Tribological Performance of Bulk Metallic Glass. *Crystals* **2022**, *12*, 748. [CrossRef]

42. Gregorčič, P.; Šetina-Batič, B.; Hočevar, M.; Šetina-Batič, B.; Hočevar, M.; Šetina-Batič, B.; Hočevar, M. Controlling the stainless steel surface wettability by nanosecond direct laser texturing at high fluences. *Appl. Phys. A* **2017**, *123*, 766. [CrossRef]

43. Li, D.; Wang, H.; Luo, D.; Liu, Y.; Han, Z.; Ren, L. Corrosion resistance controllable of biomimetic superhydrophobic microstructured magnesium alloy by controlled adhesion. *Surf. Coat. Technol.* **2018**, *347*, 173–180. [CrossRef]

44. Zhang, L.; Zhang, M.; Gao, J.; Gao, M.; Wang, X.; Li, B.; Liu, J. Study on the preparation and stearic acid modification of hydrophobic Ni625 laser cladding coating. *Mater. Lett.* **2023**, *346*, 134526. [CrossRef]

45. Yayoglu, Y.E.; Toomey, R.G.; Crane, N.B.; Gallant, N.D. Laser machined micropatterns as corrosion protection of both hydrophobic and hydrophilic magnesium. *J. Mech. Behav. Biomed. Mater.* **2022**, *125*, 104920. [CrossRef] [PubMed]

46. Cao, J.; Ma, B.; Yang, Y.; Li, L.; Li, X. Femtosecond Laser Preparation of Terracotta Warrior-like Pit Superhydrophobic Structure on Magnesium Alloy with Mechanical Durability and Corrosion Resistance. *Langmuir* **2023**, *39*, 10230–10239. [CrossRef]

47. Li, X.; Jiang, Y.; Tan, X.; Zhang, Z.; Jiang, Z.; Lian, J.; Wen, C.; Ren, L. Superhydrophobic brass surfaces with tunable water adhesion fabricated by laser texturing followed by heat treatment and their anti-corrosion ability. *Appl. Surf. Sci.* **2022**, *575*, 151596. [CrossRef]

48. Li, X.; Jiang, Y.; Jiang, Z.; Li, Y.; Wen, C.; Zhang, D.; Lian, J.; Zhang, Z. Improvement of corrosion resistance of H59 brass through fabricating superhydrophobic surface using laser ablation and heating treatment. *Corros. Sci.* **2021**, *180*, 109186. [CrossRef]

49. Wang, H.; Zhuang, J.; Qi, H.; Yu, J.; Guo, Z.; Ma, Y. Laser-chemical Treated Superhydrophobic Surface as a Barrier to Marine Atmospheric Corrosion. *Surf. Coat. Technol.* **2020**, *401*, 126255. [CrossRef]

50. Chui, P.; Jing, R.; Zhang, F.; Li, J.; Feng, T. Mechanical properties and corrosion behavior of β-type Ti-Zr-Nb-Mo alloys for biomedical application. *J. Alloys Compd.* **2020**, *842*, 155693. [CrossRef]

51. Xue, X.; Lu, L.; He, D.; Guan, Y.; Li, Y. Antibacterial properties and cytocompatibility of Ti-20Zr-10Nb-4Ta alloy surface with Ag microparticles by laser treatment. *Surf. Coat. Technol.* **2021**, *425*, 127716. [CrossRef]

52. Tong, W.; Karthik, N.; Li, J.; Wang, N.; Xiong, D. Superhydrophobic Surface with Stepwise Multilayered Micro- And Nanostructure and an Investigation of Its Corrosion Resistance. *Langmuir* **2019**, *35*, 15078–15085. [CrossRef]

53. Nahum, E.Z.; Lugovskoy, A.; Lugovskoy, S.; Sobolev, A. Synthesis of Titanium Oxide Nanotubes Loaded with Hydroxyapatite. *Nanomaterials* **2023**, *13*, 2743. [CrossRef] [PubMed]

54. Atrens, A.; Chen, X.; Shi, Z. Mg Corrosion—Recent Progress. *Corros. Mater. Degrad.* **2022**, *3*, 566–597. [CrossRef]

55. Li, Y.; Shi, Z.; Chen, X.; Atrens, A. Anodic hydrogen evolution on Mg. *J. Magnes. Alloys* **2021**, *9*, 2049–2062. [CrossRef]

56. Peng, C.; Zhang, S.; Sun, Z.; Ren, L.; Yang, K. Effect of annealing temperature on mechanical and antibacterial properties of Cu-bearing titanium alloy and its preliminary study of antibacterial mechanism. *Mater. Sci. Eng. C* **2018**, *93*, 495–504. [CrossRef] [PubMed]

57. Du, C.; Yuan, H.; Zhu, X.; Zhang, T.; Liu, Z.; Wang, C. Fabrication of antibacterial Zr-BMG biomimetic surfaces by femtosecond laser. *Surf. Interfaces* **2023**, *37*, 102740. [CrossRef]

58. Jalil, S.A.; Akram, M.; Bhat, J.A.; Hayes, J.J.; Singh, S.C.; El Kabbash, M.; Guo, C. Creating superhydrophobic and antibacterial surfaces on gold by femtosecond laser pulses. *Appl. Surf. Sci.* **2020**, *506*, 144952. [CrossRef]

59. Lutey AH, A.; Gemini, L.; Romoli, L.; Lazzini, G.; Fuso, F.; Faucon, M.; Kling, R. Towards laser-textured antibacterial surfaces. *Sci. Rep.* **2018**, *8*, 10112. [CrossRef]

60. Schwibbert, K.; Richter, A.M.; Krüger, J.; Bonse, J. Laser-Textured Surfaces: A Way to Control Biofilm Formation? *Laser Photonics Rev.* **2023**, *18*, 2300753. [CrossRef]